http://dx.doi.org/10.1016/j.oceaneng.2024.116863

Primary instability, sensitivity and active control of flow past two tandem circular cylinders

Ziyu Liu [a], Lei Zhou [b, *], Hongfu Zhang [a, **], Hui Tang [c], Zhaokun Wang [c], Fuwang Zhao [c]
[a] School of Civil Engineering and Transportation, Northeast Forestry University, Harbin, China
[b] Department of Civil and Environmental Engineering, The Hong Kong University of Science and Technology, Clear Water Bay, Kowloon, Hong Kong, China
[c] Department of Mechanical Engineering, The Hong Kong Polytechnic University, Kowloon, Hong Kong, China
[*] Corresponding author.
[**] Corresponding author.
E-mail addresses: lzhouau@connect.ust.hk (L. Zhou), zhanghongfu@nefu.edu.cn (H. Zhang)

ABSTRACT

The tandem two-cylinder configuration is frequently employed in engineering structures. Its fluid force and vortex shedding are significantly greater than those of widely studied single-cylinder because of the wake-gap interaction. To unveil the underlying mechanism and perform wake control, sensitivity analysis, the adjoint method, and global linear instability were applied to the flow past two tandem cylinders. Utilizing the sensitivity map, the optimal control location was determined. The results indicate that the most sensitive region is located behind the upstream cylinder; therefore, we implemented jet control in that location. The two-dimensional direct numerical simulation was conducted to evaluate the effects of control. The findings indicate that by applying a dimensionless jet flow velocity of 1.0 at the diagonal rear of the upstream cylinder, the fluid force can be effectively reduced with an L/D ratio of 6.0. Additionally, the control effects were evaluated at a range of Reynolds numbers between 75 and 200. Analysis using high-order dynamic mode decomposition (HODMD) reveals that the presence of the jet flow causes a backward shift in the global modes and a substantial reduction in the modal energy. This demonstrates that the jet flow effectively inhibits the occurrence of vortex shedding, resulting in a reduction in both fluid forces and vortex shedding.

Keywords: two tandem cylinders; sensitive analysis; jet control; vortex shedding;

1. Introduction

Cylinder flow control, a classical fluid dynamics problem, has been the subject of extensive and in-depth investigation by previous scholars, yielding a substantial body of research findings. However, in the realm of practical ocean engineering, cylindrical formations often manifest as multiple cylinders. Examples of such structures include oil pipelines, ocean platform columns, and ocean bridge piers. The current body of research predominantly focuses on the vortex shedding and fluid force within individual cylinders, devoting comparatively less attention to the more complex phenomenon involving vortex shedding and fluid force in configurations comprising multiple cylinders.

There are three possible arrangements for two cylinders: tandem, parallel, and staggered. Sumner et al. classified the flow surrounding two cylinders of identical dimensions into fourteen distinct flow patterns, taking into account the gap between the cylinders and the angle of the incoming flow toward the central axis.(Sumner, Richards, and Akosile 2005)

The investigation conducted by Xu et al. involved the observation of the flow around two tandem cylinders. The Reynolds number (Re) was found to be between 800 and 42000, whereas the spacing ratio (L*) was varied between 1 and 15. There are three primary classifications of vortex-shedding states in the wake. At small spacing ratios (L*=1~2), these types of shear layer separation occurred; the layer was shed directly behind the downstream cylinder. The shear layer, which became separated from the upstream cylinder, re-establishes with the cylinder downstream at moderate spacing ratios (L*=2~3). This reunification leads to the development of a symmetrical vortex between the two cylinders. Vortex shedding is observed in the cylinders both upstream and downstream when the spacing ratio is further increased (L*=3~5).(Xu and Zhou 2004)

Furthermore, a substantial body of literature exists concerning flow control measures specifically designed for cylinders. Several scholars have undertaken wind tunnel experiments and numerical simulations concerning stationary and freely oscillating wake dividers. Their findings consistently indicate that wake dividers, when mounted in suitable positions and of suitable lengths, can efficiently regulate the shedding of Karman vortices within the cylindrical wake flow. (Gerrard 1966; Cimbala and Garg 1991; Kwon and Choi 1996; Assi, Bearman, and Kitney 2009; Wu and Shu 2011)

To regulate the cylinder wake, Williams et al. implemented a drain-like jet configuration. The outcomes of the flume experiments demonstrated that the symmetric jet successfully disrupted the initial vortex shedding configuration and generated symmetric vortex shedding. (Williams, Mansy, and Amato 1992)

The control of a suction and puff wake utilizing real-time feedback from wake information was simulated by Park et al. and Min et al. using numerical simulations. The simulation results indicated that the vortex shedding in the cylindrical wake at low Reynolds numbers was substantially diminished, as were the fluctuating drag and lift. (Park, Ladd, and Hendricks 1994; Min and Choi 1999)

Using wind tunnel tests for flow field visualization, Fu and Rockwell analyzed the wake of slotted cylinders and discovered that the slots generate a jet-like flow in the wake, which disrupts the structure of the Karman vortices. (Fu and Rockwell 2005)

Baek and Karniadakis reproduced the aforementioned results with numerical simulations and identified the optimal slit widths at various Reynolds numbers. By positioning the channel outlet close to the separation point of the boundary layer in the cylinder and employing the jet to induce boundary-layer perturbation and influence the shear flow,(Baek and Karniadakis 2009) Shi and Feng achieved an equivalent substantial outcome.(Shi and Feng 2015)

To simulate cylinder slotting, Dong et al. (Dong, Triantafyllou, and Karniadakis 2008) also attempted a method involving active puff at the leeward stagnation point and active suction at the windward stagnation point. They achieved a favorable wake control result. Zhu et al. conducted numerical simulations to validate their hypothesis that two parallel thin columns could be positioned in the cylindrical wake region to obstruct axial vortex shedding. They also suggested an ideal location for the thin columns' control effect and noted that active rotation at an appropriate velocity can introduce additional momentum into the boundary layer, thereby enhancing the control effect.(Zhu et al. 2015) Additionally, Jukes and Choi conducted experiments utilizing a plasma generator arranged in the cylindrical spreading direction to control the aerodynamic forces and cylindrical wake. This method also produced excellent control results. (Jukes and Choi 2009) In recent years, several wind tunnel experiments have demonstrated that by maintaining constant suction or jet control in a variety of opening scenarios, it is possible to effectively perturb the shear layer on the surface of a cylinder using the appropriate suction or jet parameters. This allows for the manipulation of wake vortex shedding and cylindrical vortex-induced vibration. (Lin, Towfighi, and Rockwell 1995; Fransson, Konieczny, and Alfredsson 2004; Wang et al. 2016)

Prior research has predominantly focused on the regulation of vibrations induced by the circulation of fluid around a single cylinder. Nevertheless, as a result of the highly dynamic interaction between the flow within the gaps and the cylinder, the resultant fluid force and response to flow-induced vibration are significantly greater than in the co-shedding state of a solitary structure(Lin, Yang, and Rockwell 2002; Mizushima and Suehiro 2005; Sharman et al. 2005; Carmo and Meneghini 2006;

Dehkordi, Moghaddam, and Jafari 2011). As of the present moment, there have been no studies that propose a method that can adequately reduce the structural response and fluid force of two tandem circular cylinders. This study centers on the flow mechanism of a tandem arrangement of two cylinders and investigates the application of jet control to mitigate flow-induced vibration in this particular configuration.

By predicting the optimal placement of the control element to mitigate global instability through theoretical analysis utilizing sensitivity analysis-based control, it becomes simpler to design effective controls (Giannetti and Luchini 2007; Marquet, Sipp, and Jacquin 2008; Boujo 2021; Li and Zhang 2022). This approach demonstrates a high level of efficiency due to its exclusive reliance on direct global instability and adjoint calculation rather than solving for controlled flows (Giannetti and Luchini 2007; Li and Zhang 2022). Flow around a circular cylinder, square cylinder, Ahmed body, stalled airfoil, and diffusing passage have all been analyzed using this method(Meliga, Pujals, and Serre 2012; Delassaux et al. 2021; Ren, Rabault, and Tang 2021; Wang et al. 2021; Zhou et al. 2023).

The primary aim of this research is to examine the application of jet flow in the active regulation of two tandem cylinders. The concomitant method is initially employed to perform a comprehensive analysis of linear stability and sensitivity on a global scale. The sensitivity map for local feedback is acquired. By utilizing the obtained results, one can ascertain the optimal placement of the control jet. At Re = 100, the co-shedding flow conditions govern the fluid force and vortex shedding of two cylinders via a range of jet velocities. As L/D = 6.0, the cylinders are spaced apart. To compare fluid force with the baseline condition at different Reynolds numbers (Re = 75, 100, 125, 150, 175, and 200), the jet flow velocity $U_j = 1.0$ is selected and analyzed. This velocity is renowned for its exceptional control.

By applying the Higher Order Dynamic Modal Decomposition (HODMD) to the dynamic coherent modes of the system, the control mechanism of the system was uncovered(Hemati, Williams, and Rowley 2014; Le Clainche and Vega 2017; Li, Tim, and Hu 2020; Zhang et al. 2021; Dai et al. 2022; Huang, Dai, and Yang 2022; Zhang et al. 2022; Zhang, Zhou, and Tim 2022; Wen, Zhou, and Zhang 2023; Zhu et al. 2023). However, in practical engineering applications, the Reynolds number is perpetually increased. The primary factor contributing to vortex shedding and periodic fluid forces is the two-dimensional nature of periodic vortex shedding. An essential component of flow physics knowledge is the investigation of vortex-shedding control in laminar flow, which can provide precious insights into more complex vortex-shedding phenomena. (Rabiee, Barzan, and

Mohammadebrahim 2021)Moreover, an abundance of research efforts has been devoted to examining the vortex shedding or fluid forces on bluff structures in recent years.(Leontini, Thompson, and Hourigan 2007; Narendran and Jaiman 2019; Chen et al. 2021; Maceda et al. 2021; Khan et al. 2022)

2. Numerical methodology

This section establishes the optimal flow control position through the implementation of linear stability and sensitive analysis techniques. The information provided suggests that the objective of the proposed and implemented jet control strategy is to decrease the vortex shedding of two tandem circular cylinders.

2.1. Method for analyzing linear stability and sensitivity

We will conduct the linear stability analysis to study the flow stability/instability of the confined wake flow. To linearize the incompressible Navier-Stokes equations, the total flow states $(\boldsymbol{u}, p)$ are decomposed as a sum of steady base states $(\boldsymbol{U}_b, P_b)$ and infinitesimal perturbations $(\tilde{\boldsymbol{u}}, \tilde{p})$. Based on the specific problems to be analyzed below, $\boldsymbol{U}_b$ can be chosen as the mean flow or the steady-state solution to the nonlinear Navier-Stokes equations, which are called respectively the mean flow and the base flow in this work. In the linear stability analysis, the perturbations are assumed to be in the form of normal modes, where the real part and the imaginary part are the growth rate and frequency of the mode. After substituting the normal-mode into the Navier-Stokes equations and linearizing them around the base state $(\boldsymbol{U}_b, P_b)$, we obtain:

$$\sigma\hat{\boldsymbol{u}} + \nabla\hat{\boldsymbol{u}}\cdot\boldsymbol{U}_b + \nabla\boldsymbol{U}_b\cdot\hat{\boldsymbol{u}} = -\nabla\hat{p} + \frac{1}{\mathrm{Re}}\nabla^2\hat{\boldsymbol{u}}, \nabla\cdot\hat{\boldsymbol{u}} = 0 \tag{1}$$

An adjoint method-based sensitivity analysis will also be conducted as part of the present work. It is a crucial instrument that has been utilized extensively in the optimization of shape and flow control. Similar to Giannetti and Luchini(Giannetti and Luchini 2007), the adjoint equation of the Navier-Stokes equations that have been linearized is:

$$\sigma^*\hat{\boldsymbol{u}}^+ - \nabla\hat{\boldsymbol{u}}^+\cdot\boldsymbol{U}_b + (\nabla\boldsymbol{U}_b)^T\cdot\hat{\boldsymbol{u}}^+ = -\nabla\hat{p}^+ + \frac{1}{\mathrm{Re}}\nabla^2\hat{\boldsymbol{u}}^+, \nabla\cdot\hat{\boldsymbol{u}}^+ = 0 \tag{2}$$

where $\hat{\boldsymbol{u}}^+$ and $\hat{p}^+$ are the adjoint vectors to $\hat{\boldsymbol{u}}$ and $\hat{p}$ respectively. In principle, the boundary conditions for the adjoint equation are $\hat{\boldsymbol{u}}^+ = 0$ at the inlet and walls, $\hat{p}^+\boldsymbol{n} - Re^{-1}\left(\nabla\hat{\boldsymbol{u}}^+\right)\cdot\boldsymbol{n} = \left(\boldsymbol{U}_b\cdot\boldsymbol{n}\right)\hat{\boldsymbol{u}}^+$ at the outlet.

In a linear theory approach, the feedback process can be mathematically described through a relation

$$\boldsymbol{f} = \boldsymbol{C}\left(x,y\right)\boldsymbol{u} \tag{3}$$

where $\boldsymbol{C}$ is the 2 × 2 matrix of the coupling coefficients, while $\boldsymbol{u}$ and $\boldsymbol{f}$ are the velocity and the force fields. Generally, the coupling coefficients in the matrix are functions of the coordinates $\left(x,y\right)$. However, if the feedback is localized in space, we can simplify the model by assuming

$$\boldsymbol{C}\left(x,y\right) = \delta\left(x-x_0, y-y_0\right)\boldsymbol{C}_0 \tag{4}$$

where $\boldsymbol{C}_0$ is here a constant coefficient matrix, $\left(x_0, y_0\right)$ indicates the position where the feedback acts and $\delta\left(x-x_0, y-y_0\right)$ denotes the Kronecker delta function.

When the product of the adjoint and direct fields is calculated, the maximum coupling among the velocity components is achieved. Afterword, the regions where the instability mechanism operates are identified by determining where the feedback is strongest. (Giannetti and Luchini 2007)

2.2 Strategy for flow control

From present study it was ascertained that the diagonal rear section of the upstream cylinder (UC) contains the wavemaker region, while the downstream cylinder (DC) contains the wavemaker region. As illustrated in Figure 1, the jet flow utilized in this investigation was positioned diagonally to the rear of the UC, with its center oriented at a 20-degree angle to the axis. Furthermore, the jet flow was symmetrically arranged on both the top and bottom. The jet slot width was determined as $d = 0.05D$ the dimensionless flow rate of the jet $U_j = U_{jet}/U$ (referred to as the jet flow rate), which U is defined as the free-stream rate and U_{jet} the jet flow rate.

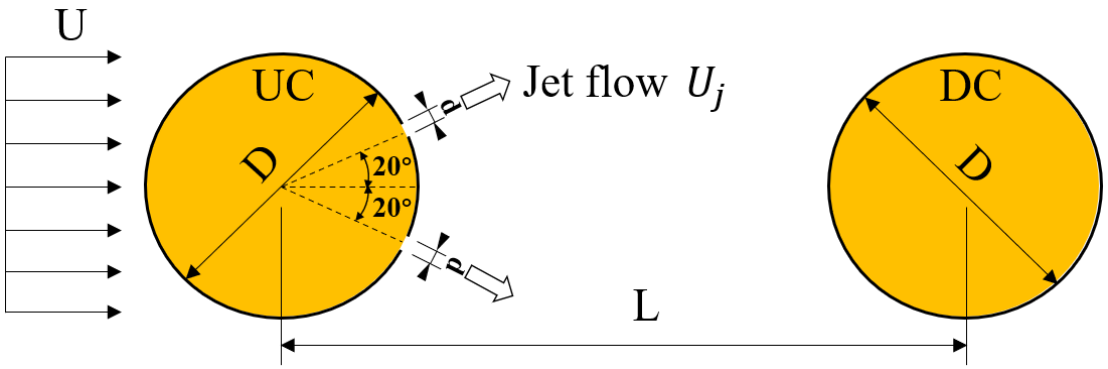

Figure 1. The jet control was situated at an oblique position to the rear of the UC.

The numerical computations were executed utilizing Fluent 19.2. The cylinder under investigation is composed of a rigid material, and its diameter is D=0.1m, the inflow velocity at U=1.0m/s, the fluid density at ρ=1.0 kg/m3, the kinematic viscous coefficient of the fluid as ν=0.001 (m^2)/s, and the corresponding Reynolds number Re=100 is calculated by the formula Re=UD/ν. To satisfy the CFL condition, which is $CFL = \frac{U\Delta t}{\Delta x} \le 0.5$, the time step is taken as Δt = 0.0005s.

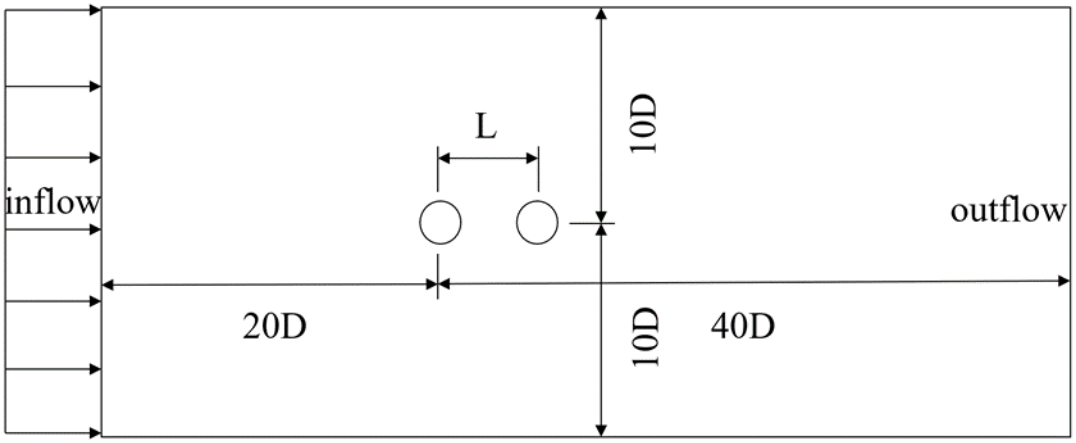

Figure 2. Schematic diagram of the computational domain

2.3 Verification and validation of the computational methods

To ascertain the soundness of the computational methods and parameters employed in this article, we initially validated the computational model's results using a stationary single cylinder characterized by a Reynolds number of 100. C_D, C_L, C_L', St are defined as the following:

$$C_D = \frac{F_D}{0.5\rho U^2 D},$$

$$C_L = \frac{F_L}{0.5\rho U^2 D},$$

C_L' is the root mean square of C_L

$$St = fD/U,$$

where F_D and F_L are the measured drag and lift forces, respectively; ρ is the fluid density; U is the free-stream velocity.

Table 1. Results validation for the fixed single-cylinder model with Re=100

	C_D	C_L'	St
Singh, S. P., & Mittal (Singh and Mittal 2005)	1.350	0.250	0.166
Sharman, B (Sharman et al. 2005)	1.330	0.230	0.164
Singha, S., & Sinhamahapatra, K. P. (Singha and Sinhamahapatra 2010)	1.431	0.226	0.165
Qu, L. Norberg, C., Davidson, L. et al. (Qu et al. 2013)	1.319	0.233	0.166
Present	1.341	0.233	0.164

The simulation results for the fixed single cylinder presented in this paper, along with the numerical simulation results previously published in the literature, are summarized in Table 1. As demonstrated by the comparison, the simulation outcomes are, on the whole, consistent.

To further validate the computational models presented in this article, at the Reynolds number of 100, the mean drag and fluctuating lift coefficient of two tandem cylinders, as well as the Strouhal number of lift force of the DC with spacing ratios L/D = 2, 4, 6, and 8, are compared to the results reported in the literature. The outcomes of the comparison are illustrated in Figure 3. The analysis of the results indicated that the mean drag and fluctuating lift coefficient of two tandem cylinders, as well as the Strouhal number of lift force of the DC in this study, were all within 5% of the values reported in the literature. Furthermore, it was observed that the trend of aerodynamic coefficients and the Strouhal number in this study remained consistent with the findings reported in the literature, even as the spacing ratio changed.

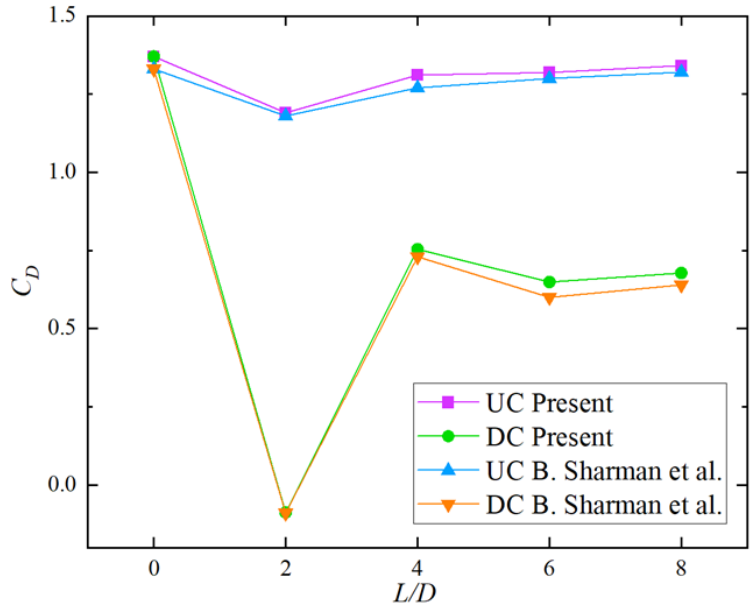

208

209 (a)Coefficient of mean drag between two tandem cylinders

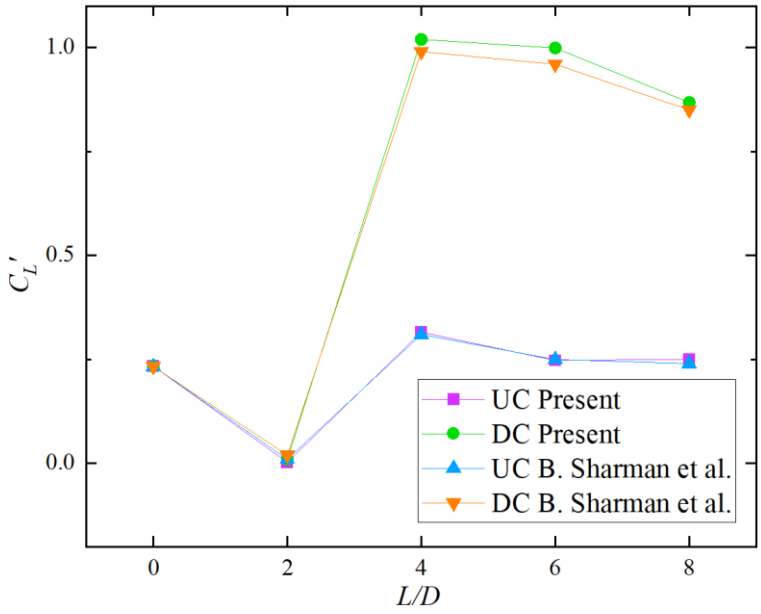

210

211 (b) Coefficient of fluctuating lift of two tandem cylinders

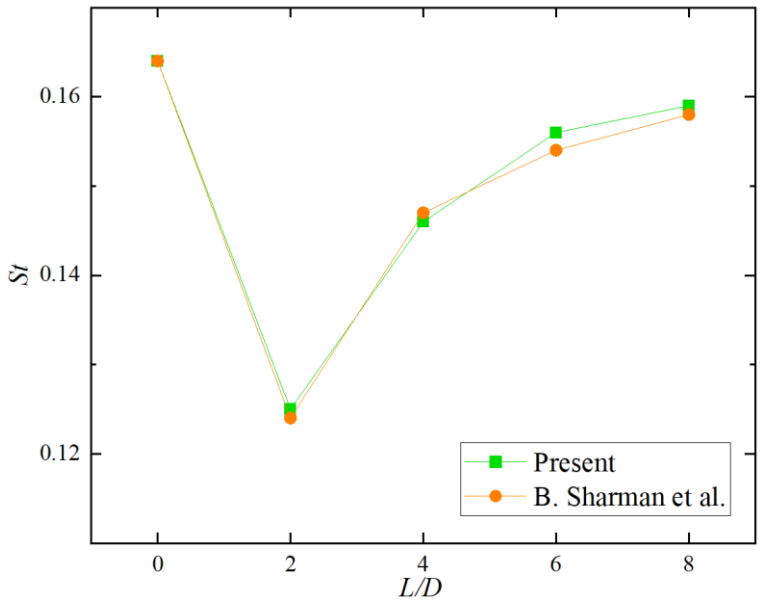

(c) Strouhal number of DC lift force

Figure 3: Validation of the results for the two tandem cylinder model

3. RESULTS AND DISCUSSION

3.1. Linear stability and sensitivity analysis

In this section, the linear stability and sensitivity analysis were employed to identify the wavemaker region of the two tandem cylinders, thus locating the region that may be most suitable for conducting flow control. Three scenarios were investigated in this analysis, at Reynolds number 60, 100, and 150, respectively.

At the outset, the fundamental stream was obtained by employing the unsteady Navier-Stokes equations at Re = 60, 100, and 150. As shown in Figure 4, the baseflow was defined as the time-averaged flow state. The steady flow field exhibits inferior performance in predicting the occurrence of vortex shedding compared to the time-averaged flow field. However, our focus remains exclusively on the wavemaker regions that are identifiable via direct and adjoint modes. Therefore, an analysis of the growth rate and frequency was not performed in the present study.

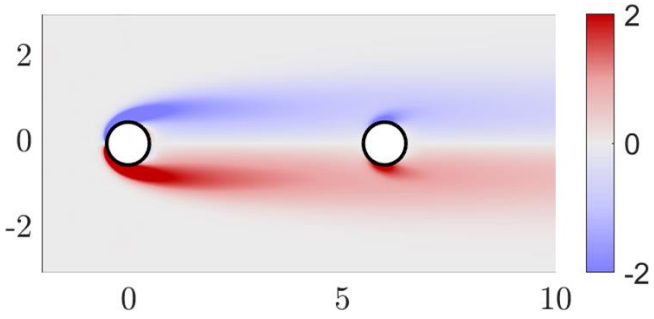

(a) L/D = 6， Re = 60

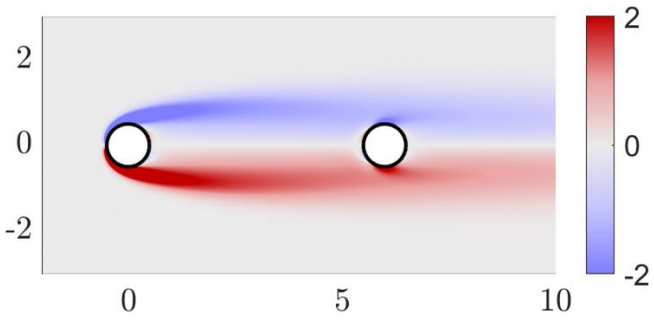

(b) L/D =6， Re = 100

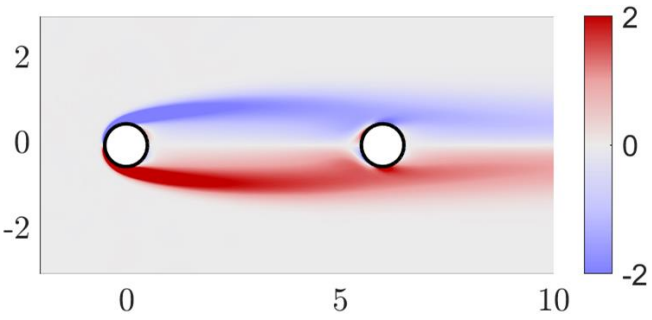

(c) L/D = 6， Re = 150

Figure 4: Baseflow vorticity at Re=60 (a), 100 (b), and 150 (c)

The direct modal plots for Re = 60, 100, and 150 at L/D = 6 are depicted in Figure 5. Except for the primary direct global mode, all modes demonstrate antisymmetric characteristics. When the Reynolds number is reduced to 60, the direct mode emerges in the downstream area between the two cylinders and progressively intensifies along the streamline-coated region. As the Reynolds number increases gradually, the sizes of the direct mode flow structures between the two cylinders diminish in both width and length, whereas they expand gradually in the downstream region of the downstream cylinder. This indicates that both the wake flow and gap flow instabilities influence global instability. Additionally, as the Reynolds number increases, the impact of the instability of the gap flow diminishes progressively.

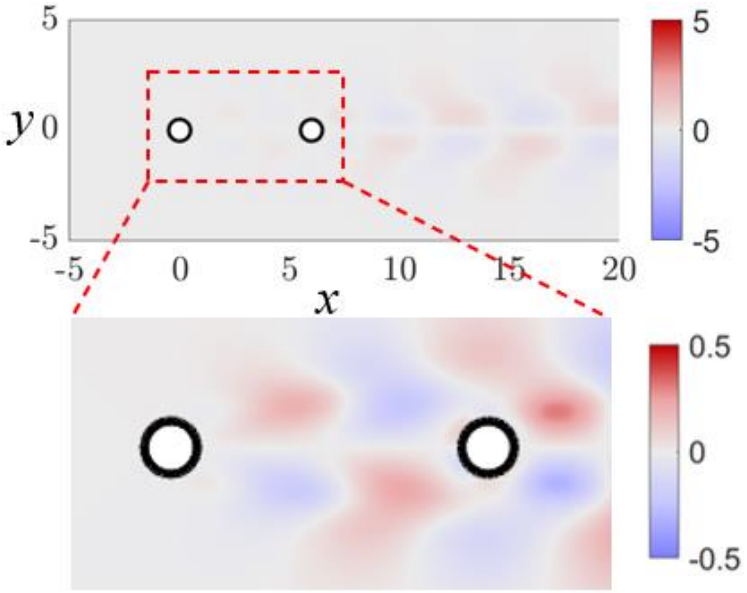

(a) L/D = 6， Re = 60

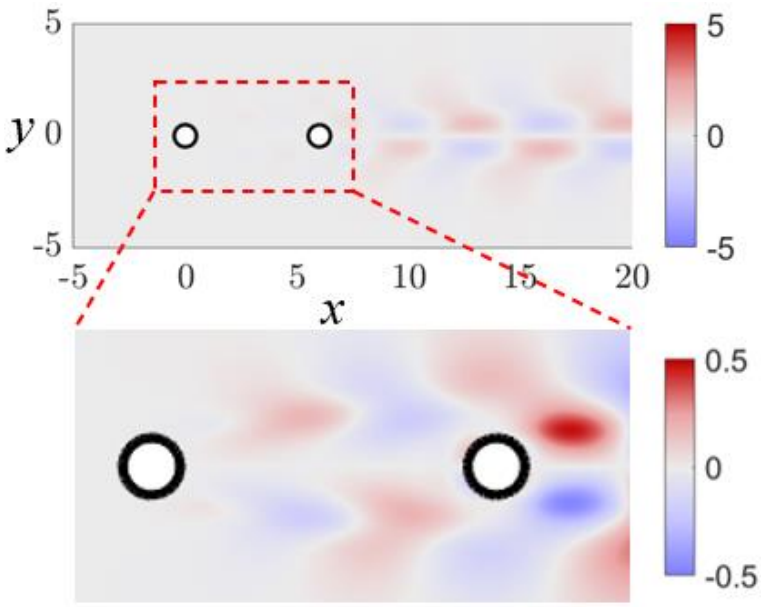

(b) L/D = 6， Re = 100

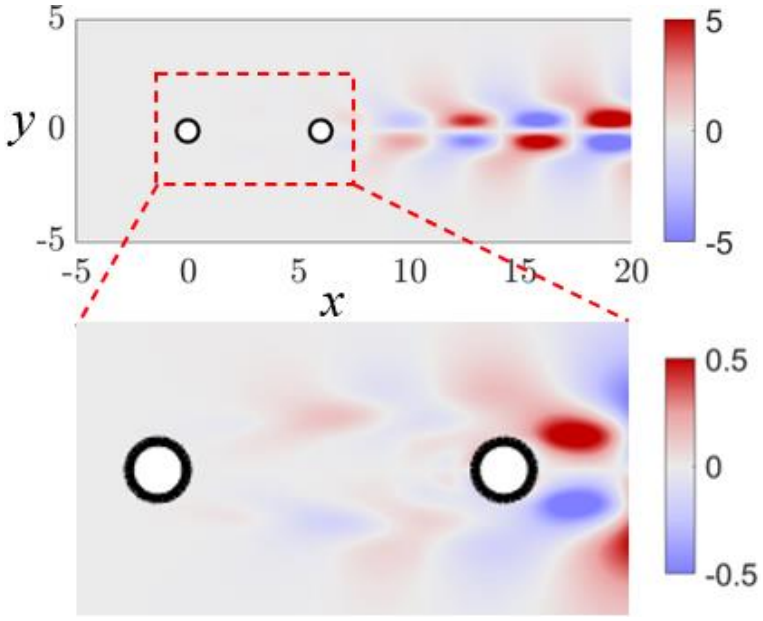

(c) L/D = 6， Re = 150

Figure 5 The leading direct global mode at Re = 60 (a), 100 (b), and 150 (c) for L/D = 6.

As shown in Figure 6, the leading direct global mode decreases as the spacing ratio between the two cylinders increases. Simultaneously, the leading direct global mode gradually manifests itself in the region bounded by the two cylinders. This indicates that the effect of the instability at the gap between the two cylinders increases in tandem with the spacing ratio between the two cylinders.

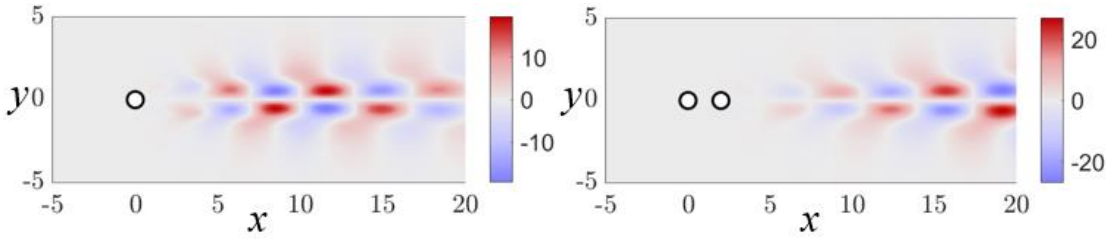

(a) single cylinder (b) L/D =2

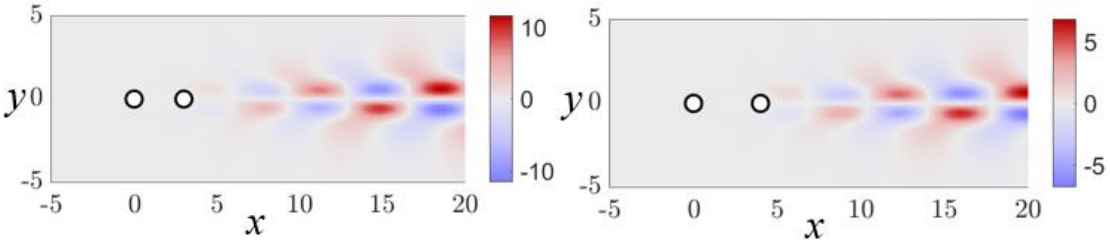

(c) L/D=3 (d) L/D =4

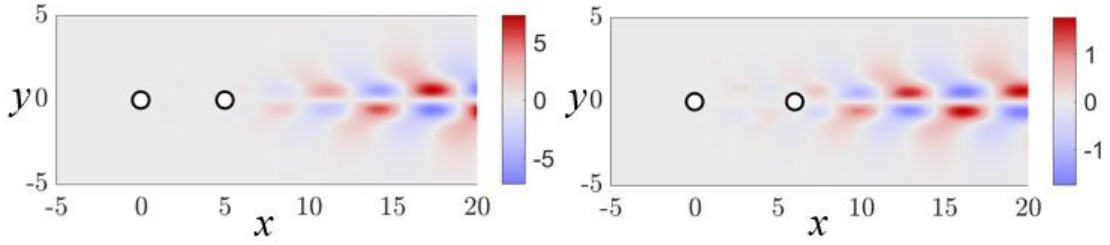

(e) L/D=5 (f) L/D=6

Figure 6 illustrates the leading direct global mode for Re = 100 (a) and tandem cylinders with L/D = 2 (b), 3 (c), 4 (d), 5 (e), 6 (f)

The adjoint modes serve as a direct indicator of the momentum imposition sensitivity of the flow structures. The adjoint modes of streamwise velocity exhibit a symmetric pattern that is similar to that of the direct modes. The adjoint modes at Re = 60, 100, and 150 are essentially identical. As the Reynolds number increases gradually, there is a corresponding decrease in the range of the adjoint modes and the overall value of the modes. Nevertheless, the area with the greatest susceptibility to momentum forcing is confined to both transverse portions of the UC. Consequently, the vicinity of the UC is a critical flow control location.

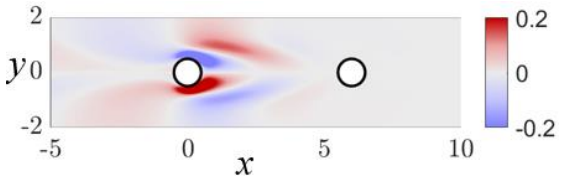

(a) L/D=6， Re = 60

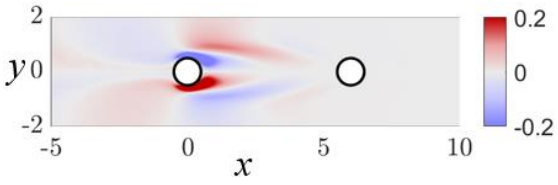

(b) L/D= 6， Re = 100

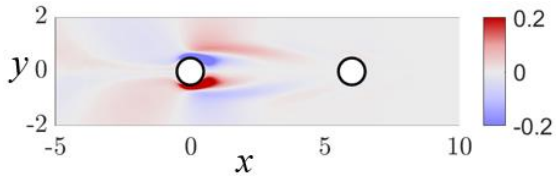

(c) L/D=6， Re = 150

Figure 7. The adjoint mode at Re = 60 (a), 100 (b), and 150 (c) for L/D = 6.

The adjoint modes are primarily concentrated on both sides of UC, as shown in Figure 8. One can locate the region with the greatest susceptibility to momentum forcing near the UC. In situations where the distance between the two cylinders is minimal, the DC sides also manifest substantial accompanying modes. However, as the spacing ratio between the two cylinders increases, the adjoint modes on both sides of the DC diminish gradually. Changes in adjoint modes are the only ones on either side of the UC that lack clarity. This implies that irrespective of the spacing ratio between the two cylinders, the vicinity of the UC is a critical location for flow control.

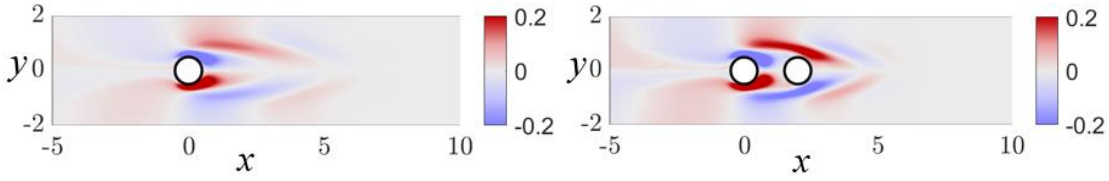

(a) single cylinder (b)L/D=2

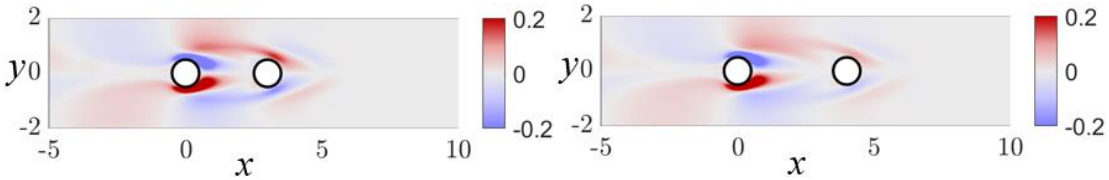

(c) L/D=3 (d) L/D=4

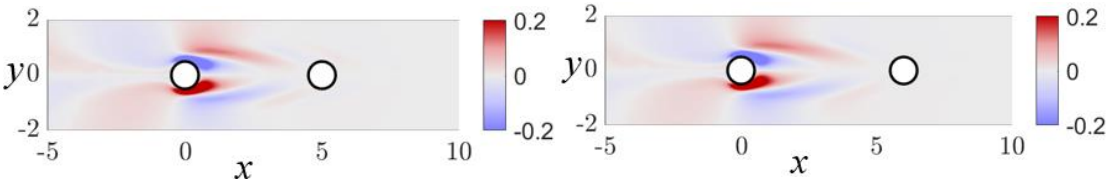

(e) L/D=5 (f) L/D=6

Figure 8 illustrates the adjoint mode for Re = 100 at single cylinder (a) and tandem cylinders with

L/D = 2 (b), 3 (c), 4 (d), 5 (e), 6 (f)

The sensitivity map to local feedback for L/D=6 at Re = 60, 100, and 150 is presented in Figure 9., which illustrates the spatial impact of perturbations on the flow field. A noticeable absence of regions exhibiting heightened sensitivity is observed in the DC, whereas the majority of regions with increased sensitivity are located downstream of the UC. This suggests that the flow pattern encircling the DC exhibits reduced responsiveness in impeding the removal of wake vortices. The main distribution remains unchanged as the Reynolds number increases, causing the dimensions and maximum value of the more sensitive region to decrease. Significantly, the increased Reynolds number resulted in a rise in sensitivity near the DC, while it remained below the UC.

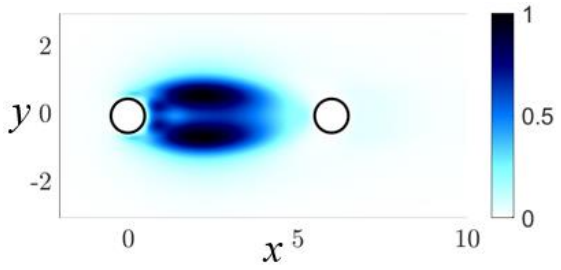

(a) L/D = 6， Re = 60

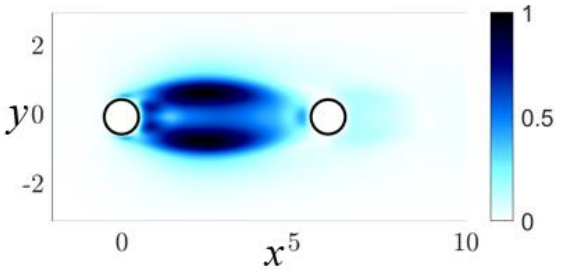

(b) L/D= 6， Re = 100

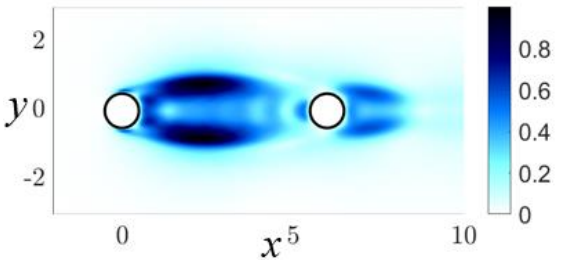

(c) L/D=6， Re = 150

Figure 9. Local feedback sensitivity map for L/D = 6 at Re = 60 (a), 100 (b), and 150 (c)

As illustrated in Figure 10, when the spacing ratio between the two cylinders is small and the Reynolds number is 100, the region of greater sensitivity is situated in the rear of the DC. Nevertheless, with an increase in the spacing ratio between the two cylinders, the area characterized by greater sensitivity progressively transitions from the vicinity of the DC to the wake region of the

UC. Furthermore, in the case of wake vortex shedding suppression with a larger spacing of two cylinders, the rear region of the UC is most susceptible to local feedback. As a result, it is advisable to position the jet flow in the rear of the UC.

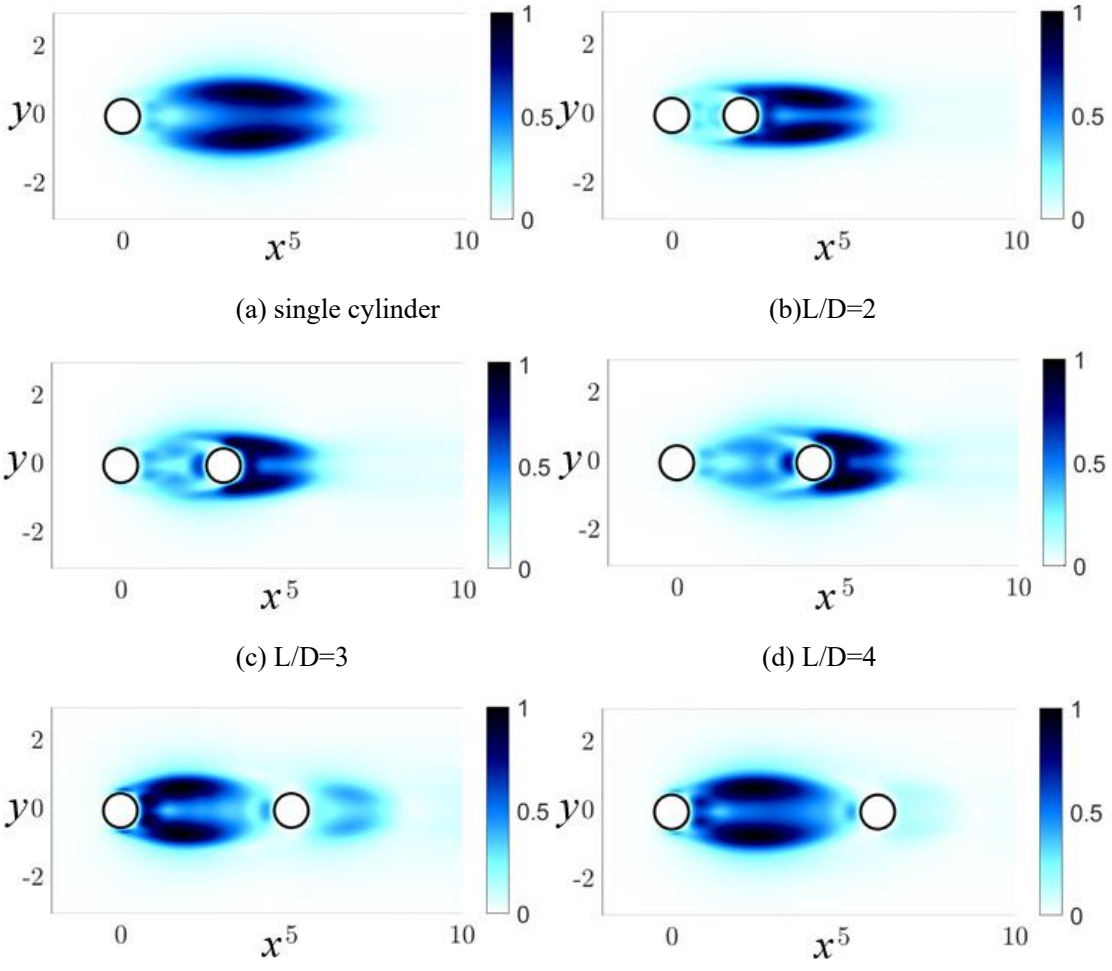

(a) single cylinder (b)L/D=2

(c) L/D=3 (d) L/D=4

(e) L/D=5 (f) L/D=6

Figure 10.The sensitivity map for local feedback for Re = 100 at single cylinder (a) and tandem cylinders with L/D = 2 (b), 3 (c), 4 (d), 5 (e), 6 (f)

3.2 Tandem two cylinders without jet control

To commence, a numerical simulation was conducted on a tandem of two cylinders without jet control , which serves as the baseline case. The spacing ratios in Figure 11 illustrate the mean drag and fluctuating lift coefficients of the two cylinders. Comparable in mean drag coefficient to the single cylinder is the UC. In contrast to UC, the mean drag coefficient of DC is significantly lower than that of a single cylinder, even when the spacing ratio between the two cylinders is substantial. This suggests that the inclusion of UC diminishes the mean drag coefficient of DC. When the spacing ratio is small (L/D=2), the mean drag coefficient of the DC is negative. This indicates that

the fluid is pushing the cylinder forward. Subsequently, the drag coefficient experiences a significant increase before leveling off. Furthermore, the fluctuating lift coefficients of the two cylinders approach zero. The UC's fluctuating lift coefficient subsequently approaches that of a single cylinder before leveling off. However, the DC's fluctuating lift coefficient increases until it reaches a significant value, after which it gradually decreases. This suggests that the impact of the UC wake on the DC is substantial, although the magnitude of this effect decreases as the spacing ratio increases. For flow control, we opted for the L/D=6 case (co-shedding flow regime), which exhibited mean drag fluctuations that were relatively stable and a lift coefficient that fluctuated.

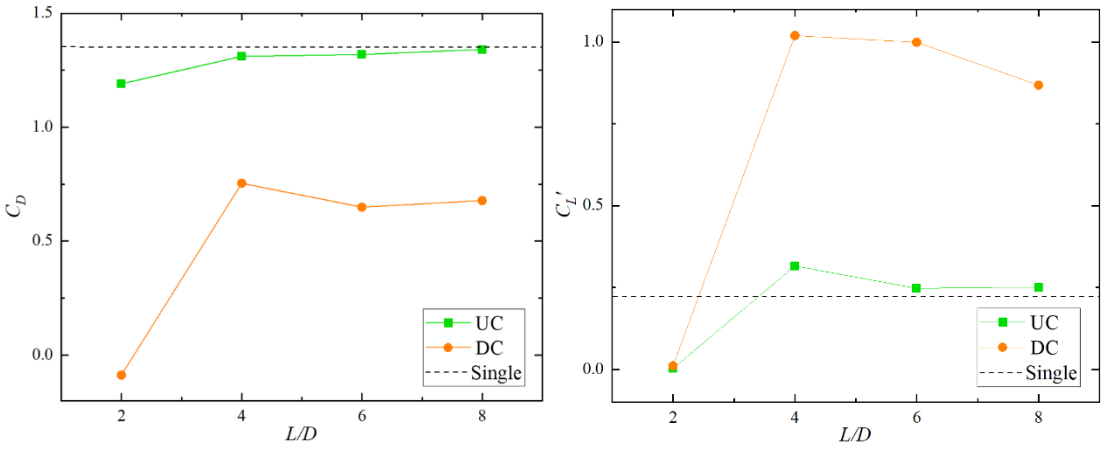

(a) Mean drag coefficient (b) Fluctuating lift coefficient

Figure 11. Coefficient of fluid force for tandem two-cylinders without jet control

3.3 Tandem two cylinders with jet control

3.3.1 Mean drag and fluctuating lift coefficient

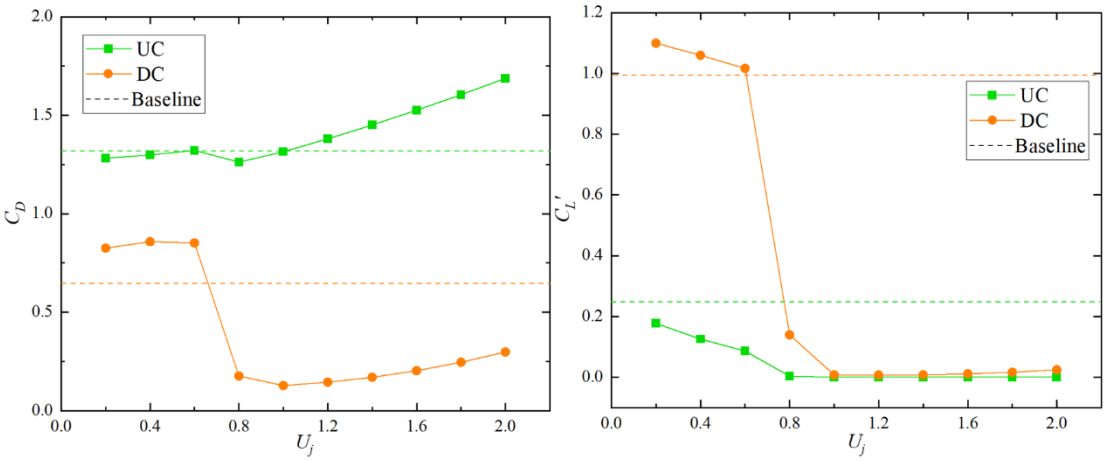

(a) Mean drag coefficient (b) Fluctuating lift coefficient

Figure 12. Coefficient of fluid force between the two cylinders as the jet flow velocity varies

An analysis was conducted on numerical calculations using various jet velocities in the conditions Re=100 and L/D=6. The fluid force coefficient of the two cylinders is illustrated in Figure 12. The results indicate that the mean drag coefficient of DC is less than that of UC due to the shading effect of UC on DC. At $U_j = 0.8$, the mean drag coefficient of DC decreases sharply, and there is a small decrease in the mean drag coefficient of UC. It is minimized at $U_j = 1.0$, and the mean drag coefficient of the two cylinders gradually increases with the increase of the jet velocity. Since the jet control is applied behind the UC, the UC has almost no drag reduction effect, whereas the DC has a significant drag reduction effect. In the C_L' plot, the baseline case has a considerably higher fluctuating lift coefficient for DC than that for UC because of the turbulent wake shedding caused by the flow through the gap. In $U_j = 0.8$, a situation similar to the C_D results occur for C_L', The significant decrease in C_L' for UC and DC indicates that the vortex shedding is stabilizing. To summarize, the jet is capable of suppressing violent vortex shedding (as proved by the flow structure analysis below), thereby reducing C_D and C_L'.

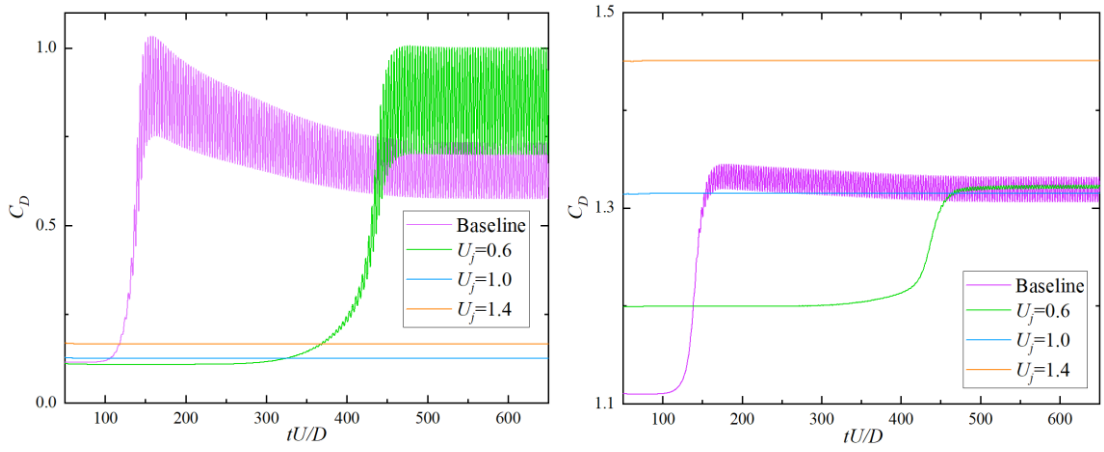

(a)DC (b)UC

Figure 13. Time history of drag coefficients in different jet velocities of DC (a) and UC (b)

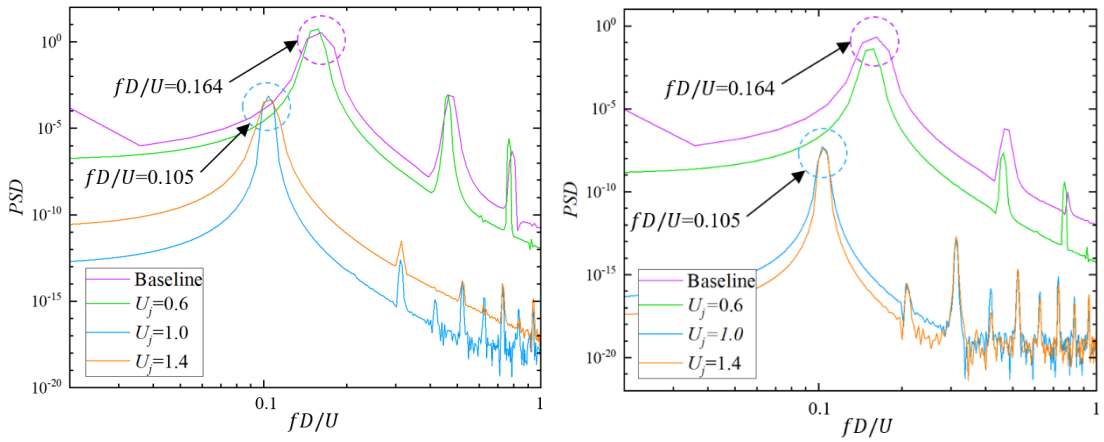

(a)DC (b)UC

Figure 14. Power spectral density of lift coefficients of DC (a) and UC (b)

As the jet velocity increases, the mean and pulsation drag of the two cylinders decreases, as illustrated in Figure 13. Also prolonged is the time between the initial condition and the stable state. The peak value of the fluctuating lift's PSD also decreases substantially as the jet velocity increases, as shown in Figure 14. As a result, vortex shedding was significantly reduced. Furthermore, when the jet velocities were high ($U_j = 1.0$ and $U_j = 1.4$), the vortex shedding frequency (fD/U) decreased from 0.164 to 0.105, indicating a delay in weak vortex shedding as well.

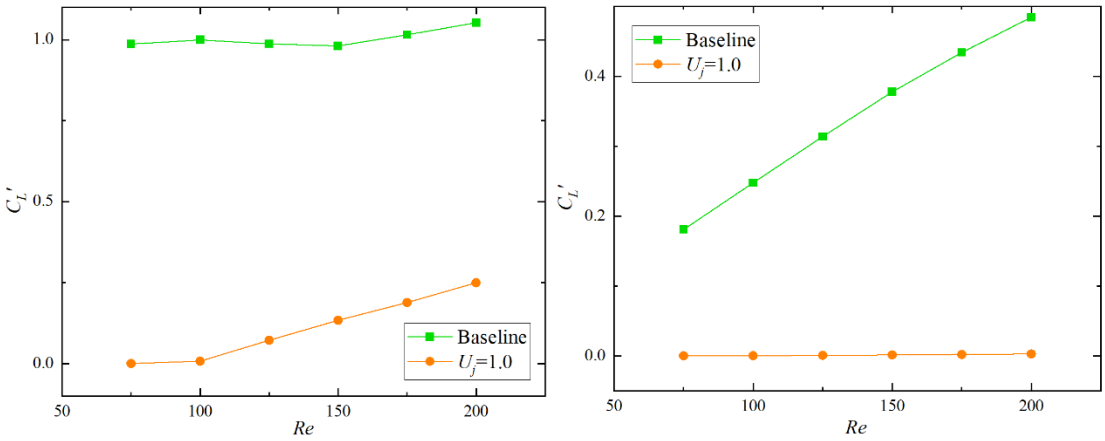

(a)DC (b)UC

Figure 15. Mean drag coefficients at different Reynolds numbers for $U_j = 1.0$ of DC (a) and UC (b)

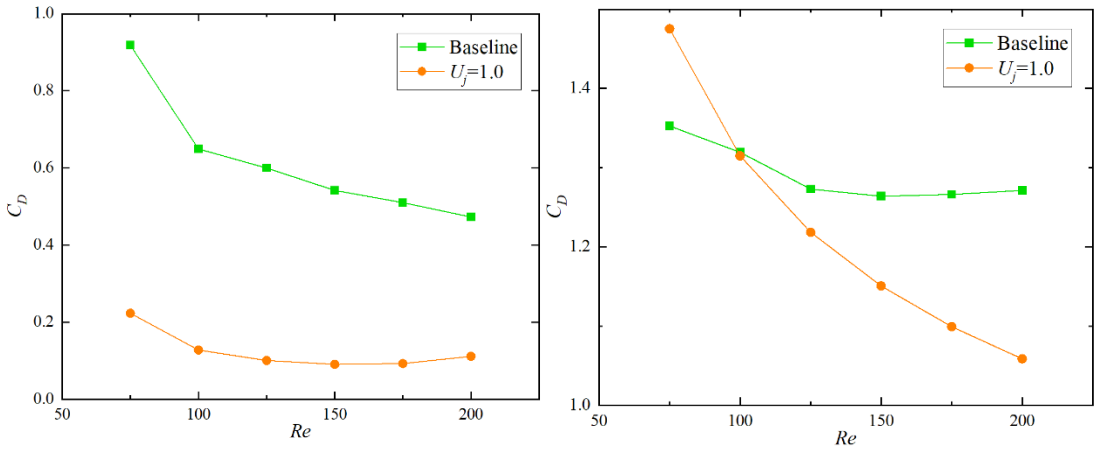

(a)DC (b)UC

Figure 16. Fluctuating lift coefficients at different Reynolds numbers for $U_j = 1.0$ of DC (a) and UC (b)

We found that $U_j = 1.0$ has the best control effect at Re=100 and L/D=6, so we selected the $U_j = 1.0$ case for comparative analysis of the flow control effect at different Reynolds numbers (Re=75, 100, 125, 150, 175, 200). The comparison results are shown in Figures 15 and 16. Firstly, the mean drag coefficients at $U_j = 1.0$ were compared with the baseline case. It can be observed that the mean drag coefficients of the DC are all reduced, while for the UC, the mean drag coefficients are reduced to varying degrees, except for the case of Re=75. Then, the fluctuating lift coefficient at $U_j = 1.0$ was compared with the baseline case. Under the influence of the jet flow, the lift coefficient of UC approaches zero, suggesting that vortex shedding takes place minimally in the region between UC and DC. Furthermore, it can be observed that the lift coefficient of the DC increases gradually with the Reynolds number when jet control is present. This indicates that vortex shedding is also commencing to manifest gradually in the DC, albeit with consistently lower lift coefficients compared to the baseline scenario. The jet flow regulation remains operational. Furthermore, it is possible to establish that the jet flow with $U_j = 1.0$ suppresses violent vortex shedding in both the gap and the wake at different Reynolds numbers, thus reducing C_D and C_L'.

3.3.2 Flow structures

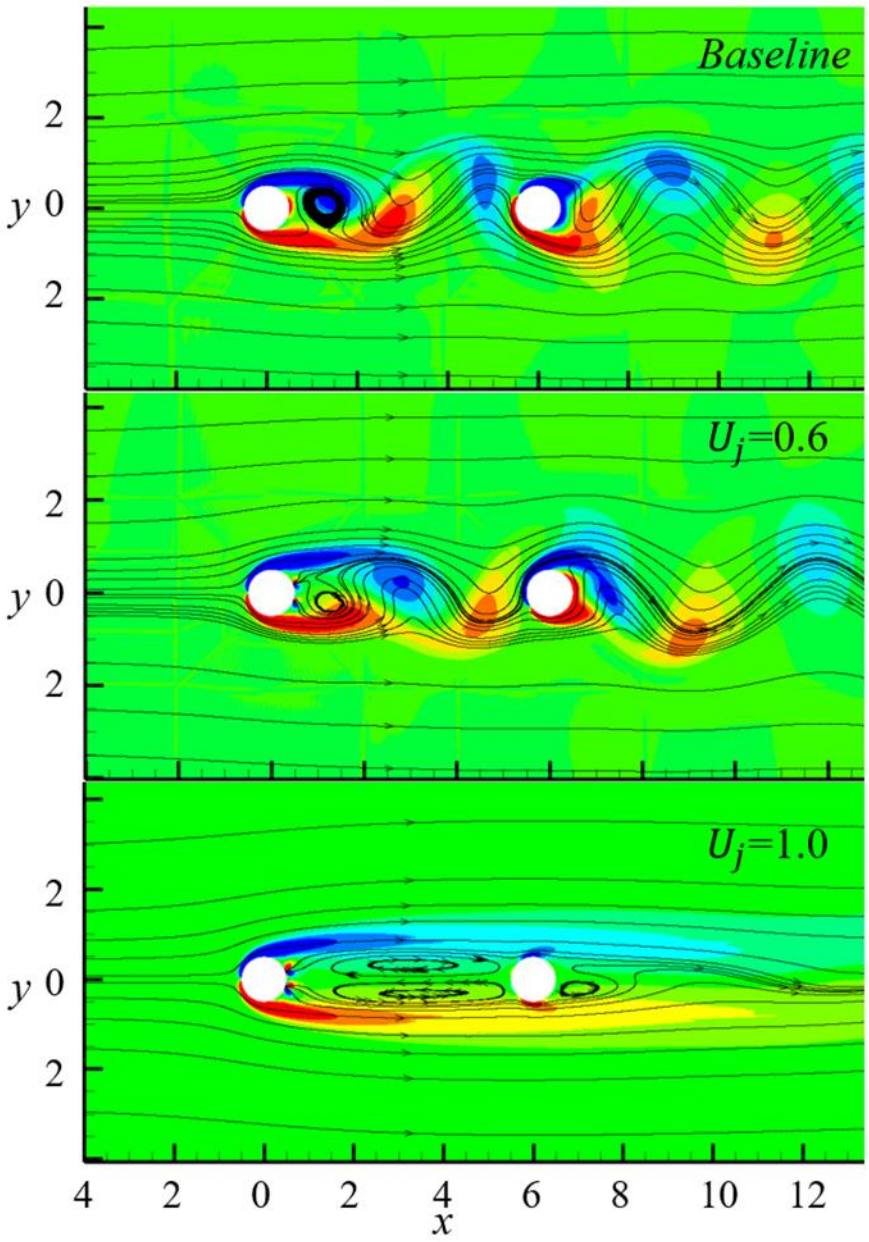

Figure 17. Structures of instantaneous flow in various jet flow velocities

Figure 17 illustrates the instantaneous flow structures for the baseline case, $U_j = 0.6$ and $U_j = 1.0$ jet control cylinders so that the intricacies of the flow fields in these two scenarios can be comprehensively comprehended. In the baseline case, vortex shedding is observed at both the gap and wake. Additionally, the vortex shedding exhibits an S shape. The gap vortex produced by the UC interacts strongly with the DC, in contrast to the single cylinder, thereby intensifying the wake vortex following the DC. This is the primary cause of the significant variations in DC's lift. By

applying the jet flow to the rear of the UC, vortex shedding in the gap and near-wake regions was effectively eliminated. In the region between the gaps, the flow structures become symmetrical and smooth. As a result of the jet flow eliminating the shear layers from the UC surface adjacent to the wake, the vortex is disrupted and a stable flow structure is produced.

We found the article related to experiments with single cylinder and compared to the experiments of the vorticity contours. Similar to their results, the jet control cannot completely suppress the vortex shedding at low jet velocities, and have better effects at high jet velocities.(Gao et al. 2019)

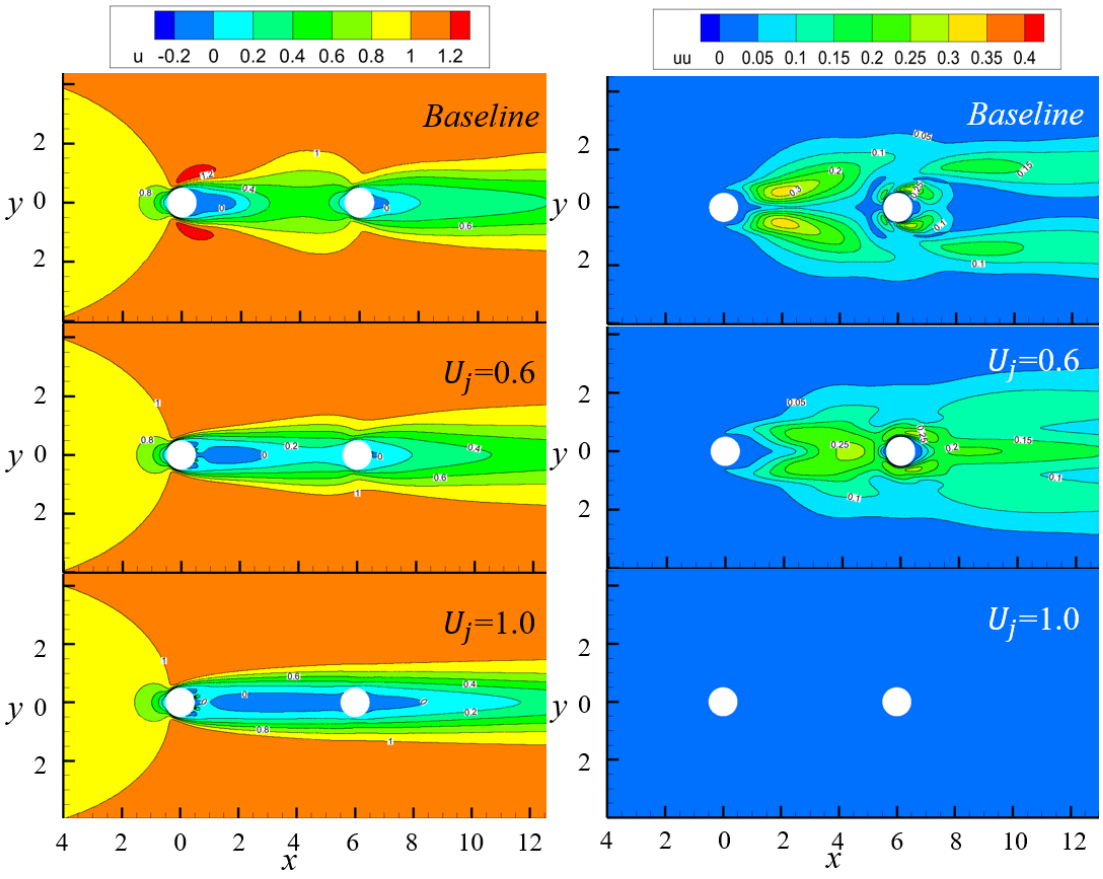

(a)The mean streamwise velocity (b)RMS of the streamwise velocity

Figure 18 Contours of mean streamwise velocity (a) and RMS of the streamwise velocity (b) for various jet flow velocities

The contours of the mean and RMS streamwise velocity for different jet velocities (including the baseline case, $U_j = 0.6$ and $U_j = 1.0$) are illustrated in Figure 18. Because of the fluid forces, the duration of vortex formation on a bluff body is significantly altered. The length of the vortex formation behind the UC marginally increased in response to the increased jet flow velocity, whereas the recirculation region behind the DC underwent a significant decrease. The correlation between the flow pattern and the velocity of the jet is readily apparent. The recirculation area shifted

419 away from the far wake (UC) and became significantly longer when the jet flow velocity was
420 increased to $U_j = 1.0$ in comparison to the baseline case. Reverse flow is not detected near the UC.
421 The results indicate that the recirculation region ceased to exist beyond the DC, resulting in pressure
422 equilibrium between the front and rear of the UC. Consequently, DC's drag approached zero.
423 For bluff bodies, the maximum value of u_{rms} is always at the roll-up position of the shear layer. The
424 fluid forces have a strong correlation with the wake width, which can be calculated using the lateral
425 distance between the two maximums u_{rms} of the DC. A greater fluid force is typically associated
426 with a wider wake. For the baseline case, the high values of u_{rms} are concentrated in the wakes of
427 UC and DC. In the baseline case, the maximum value of u_{rms} is greater than that at the gap and
428 wake, and it is highest at the trailing edge of the DC. This observation suggests a significant
429 interaction between the gap vortex produced by the UC and the shear layer of the DC. Additionally,
430 it demonstrates that the DC exhibits a greater magnitude of fluctuating lift compared to the UC. In
431 contrast to the baseline case, as the jet flow velocity increases to $U_j = 0.6$, the u_{rms} pattern
432 becomes more concentrated, particularly in the vicinity of DC.
433 This is consistent with the findings presented in Figure 11. It indicates that the fluid forces in the
434 DC do not exhibit any enhancement when compared to the baseline case. As the velocity of the jet
435 is increased further, to $U_j = 1.0$, u_{rms} approaches zero. The global flow reaches a steady state in
436 this instance, indicating that the fluctuating force approaches zero. This is illustrated in Figure 11.

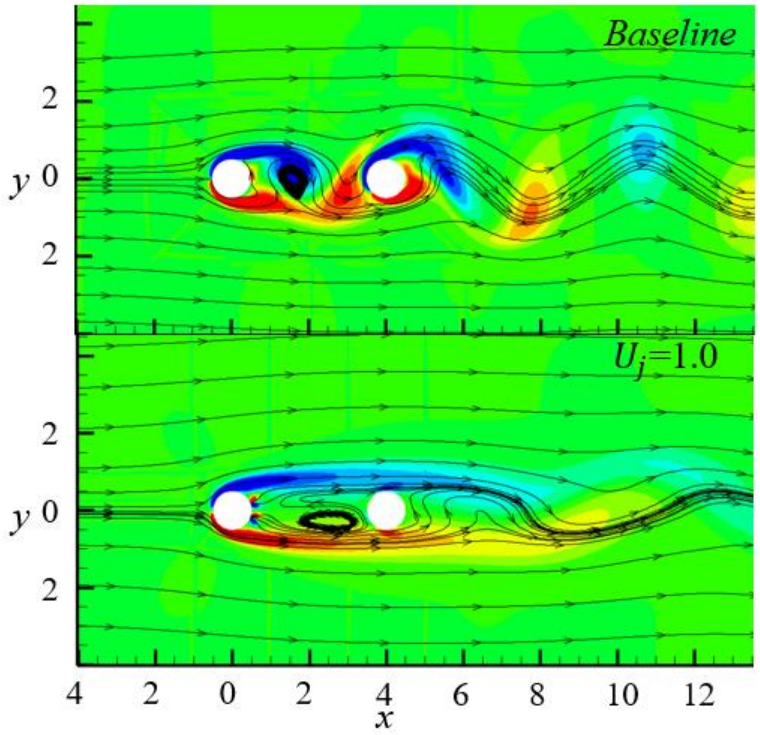

Figure 19. Structures of instantaneous flow for L/D = 4 in various jet flow velocities

The flow structure of the baseline case and $U_j = 1.0$ were observed at L/D = 4 gap ratio. Similar to the case of L/D = 6, the baseline case showed Karman vortex shedding at the gap and wake. When the jet flow with $U_j = 1.0$ was applied to the back of the UC, the vortex shedding in the gap region and near the wake region is effectively eliminated.

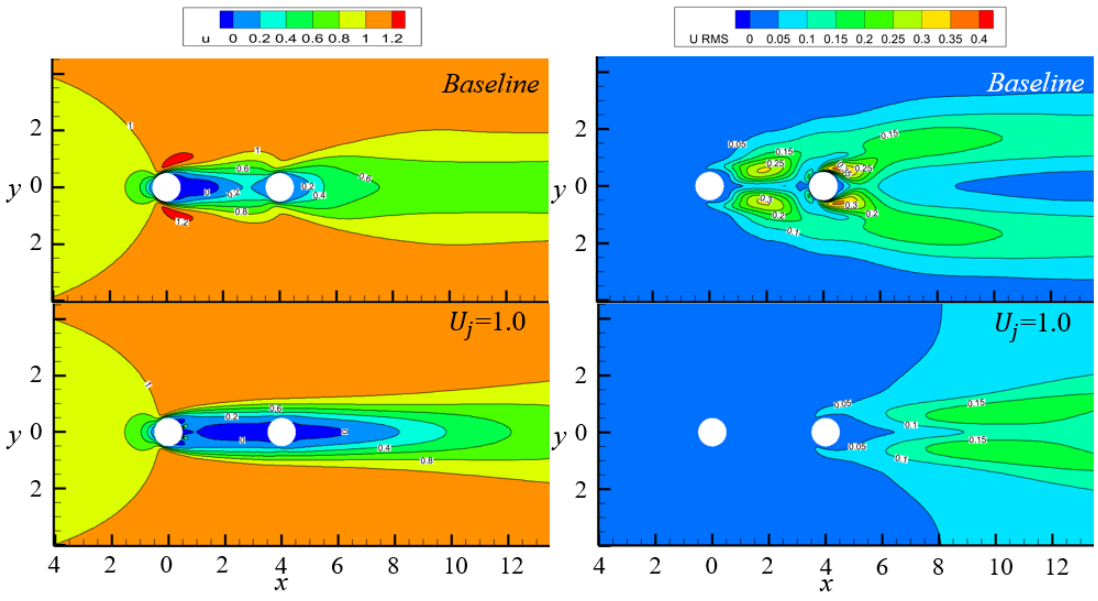

(a)The mean streamwise velocity (b)RMS of the streamwise velocity

Figure 20 Contours of mean streamwise velocity (a) and RMS of the streamwise velocity (b) in

various jet flow velocities for L/D=4

Contours of streamwise velocity for L/D =4 are also similar to the case with L/D = 6. Compared to the baseline case, the wake becomes slenderer after applying the jet control, which indicates that the flow structure is more stable. In the baseline case, the high values of u_{rms} are concentrated in the wakes of UC and DC, the maximum value of u_{rms} is greater than that at the gap and wake, and it is highest at the trailing edge of the DC. When the jet flow with $U_j = 1.0$, the u_{rms} decreases to approach zero, and the global flow reaches a steady state in this instance. The C_L' decreases 99.8 percent for UC and 93.8 percent for DC, which proves the feasibility of the jet control in various gap ratios. For smaller gap ratio case (L/D=2), the flow structure is already stable from Figure 11, so no jet control is required for this case.

3.3.3 Coherence modes

Based on the preceding sections, it is evident that the disparity between the $U_j = 0.6$ case and the baseline case is not substantial. Consequently, this section exclusively examines the flow structures for the baseline and $U_j = 1.0$ case at Re = 100 utilizing the HODMD. To guarantee the precision of the data, the extraction of all information occurred during a steady-state flow field. The dataset comprises forty complete cycles of vortex shedding. 25 snapshots are captured during each vortex shedding period. Consequently, the time interval between snapshots is denoted as T/25, where T is the duration of vortex shedding. At a time when the flow exhibited consistent fluctuations, each of the eigenvalue standards attained a value of 1.0. As depicted in Figure 21, the prevalent Ritz coefficients were consequently dispersed along a circular unit. The primary coherent and global mode energies, as well as their relationship to fluid forces, are discussed in this section.

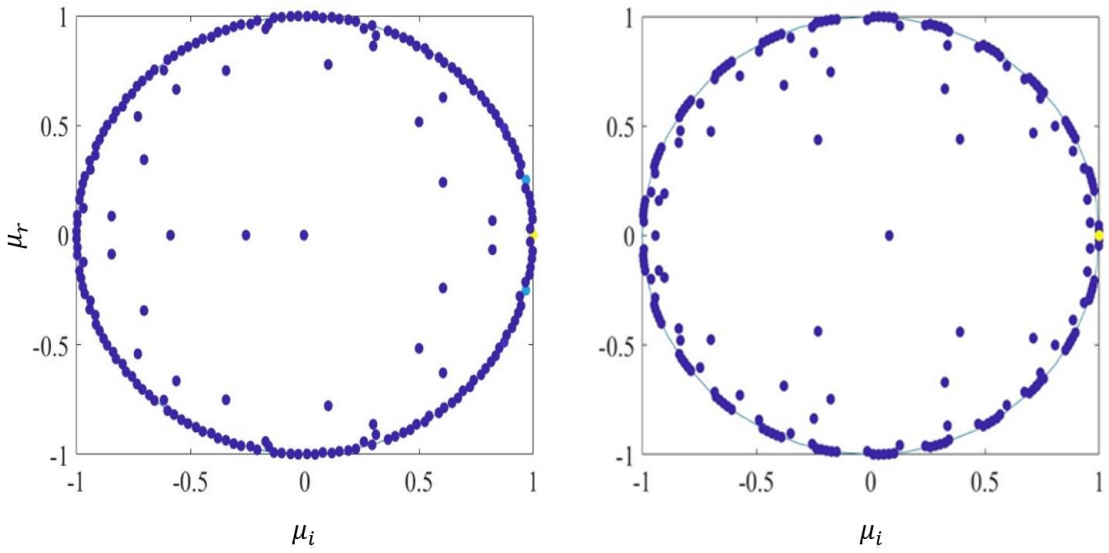

(a) baseline case (b) $U_j = 1.0$

Figure 21. Ritz values vs. unit circle for baseline case (a) and $U_j = 1.0$ (b)

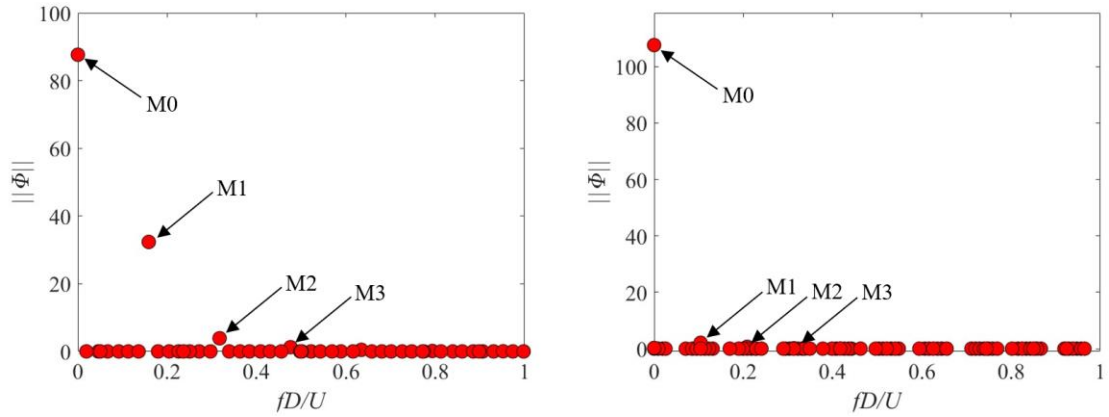

(a) baseline case (b) $U_j = 1.0$

Figure 22. Mode energy as a function of frequency for baseline case (a) and $U_j = 1.0$ (b)

The mode energy as a frequency function for the baseline case and $U_j = 1.0$ is illustrated in Figure 22. Maximum modal energy is observed at fD/U = 0 in the two cases of interest; this value corresponds to the time-averaged modes and is represented by M0. As illustrated in Figure 20, the wake for the baseline case is predominantly composed of one primary mode (M1) and two super-harmonic modes (M2, M3). The determination of these dynamic modes is predicated on the nondimensional frequencies (M1:fD/U＝St; M2:fD/U＝2St; M3:fD/U＝3St). The super-harmonic mode exhibits considerably lower energies in comparison to the primary modes, which is consistent

with the PSD results depicted in Figure 14. At a jet flow velocity increase to $U_j = 1.0$, the modal energy diminishes considerably for M1 and is nearly nonexistent for M2 and M3. Consequently, the jet flow has the potential to induce a substantial decrease in dynamic mode energy.

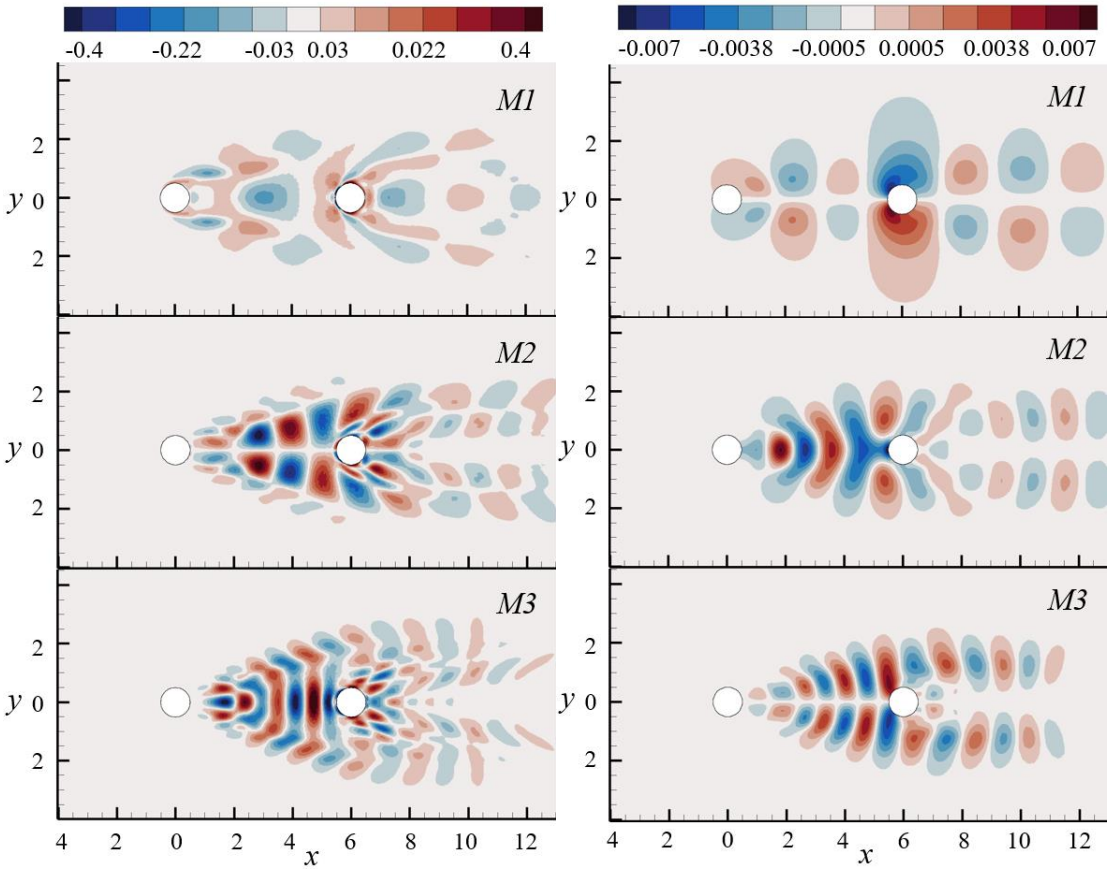

(a) Vorticity modes for baseline case (b) Pressure modes for baseline case

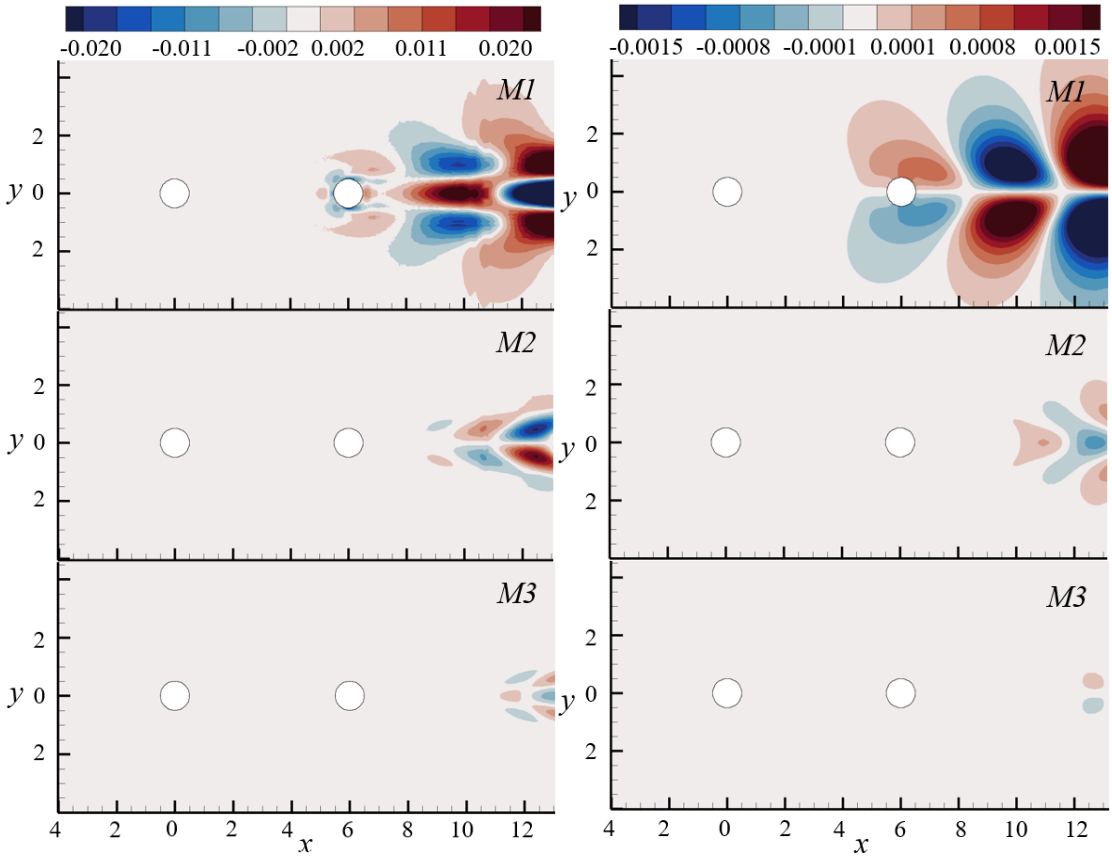

(c) Vorticity modes for $U_j = 1.0$ (d) Pressure modes for $U_j = 1.0$

Figure 23. Vorticity modes (a), (c) and pressure modes (b), (d) for baseline case and $U_j = 1.0$

Regarding the vorticity modes illustrated in Figure 23. It is determined that the vorticity modes exhibit symmetry for odd orders and antisymmetric for even orders (see Figure 23(a) and (c)). The primary mode M1 is present in both the gap and the wake for the baseline case depicted in Figure 23(a). This mode is symmetrical to the centerline of the two cylinders and exhibits a strong correlation with the lift. Furthermore, it should be noted that DC is flanked by two vortices that rotate in the same direction as UC. Consequently, the fluctuating lift on DC is more pronounced than that on UC. The antisymmetric vorticity mode of the M2 mode indicates that the vortices in the upper and lower portions produce opposing effects. This implies that the torque's effects are mutually reinforcing and do not play a role in the vortex shedding. In a similar vein, the M3 mode exhibits a symmetric form of vorticity identical to that of the M1 mode; however, its global impact is diminished as a result of its smaller mode energy. For the case of $U_j = 1.0$ in Figure 23(c), in contrast to the baseline case, it is evident that the modes undergo a substantial backward shift in their entirety, with the modes located in the gap nearly entirely disappearing. This finding suggests

501 that there is no vortex shedding occurs in the region between the UC and DC, and the vortex
502 shedding in the rear of the DC is not significant. These results are generally consistent with the
503 information presented in Figure 17, which depicts the instantaneous flow structures.

504 Regarding the pressure modes illustrated in Figure 23. It is observed that the initial three pressure
505 modes are antithetical to the vortex modes, as depicted in Figure23 (b) and (d). This indicates that
506 M1 and M3 have an asymmetrical shape, whereas M2 has a symmetrical shape due to the distinction
507 in the mode of action of the torque and force. Figure 23(b) illustrates the pressure modes for the
508 baseline case. The pressure action points in M1 and M3 are concentrically located on opposing sides
509 of DC. This indicates that the lift confidence on DC is considerably greater than that on UC, which
510 is consistent with C_D and $C_L{}'$ of the two cylinders, as shown in Figure 12. Different from the
511 baseline case, for the case $U_j = 1.0$ in Figure 23(d), the pressure and vorticity modes exhibit a
512 substantial inward shift in comparison to the initial condition. The modes vanish virtually entirely
513 within the UC and DC gaps. This supports the depiction of instantaneous flow structures in Figure
514 17.

4. Conclusions

The present study investigates the fluid forces and vortex shedding of tandem two-cylinder. The jet flow's location was determined through the linear stability sensitivity analysis. Using various jet velocities, the control mechanisms and effects of L/D = 6.0 tandem two-cylinders operating in the co-shedding flow regimes at Re = 100 were investigated. Then, we selected the case of $U_j = 1.0$, which has superior control effects, and examined the control effects for various Reynolds number scenarios with L/D = 6.0.

The structure's sensitivity indicates that the wavemaker region is exclusively located in the area immediately posterior to the UC. It has been demonstrated that the effect of flow sensitivity in inhibiting wake vortex shedding is diminished in the vicinity of DC. As a result, the location of the jet flow is posterior to UC. As the velocity of the jet increased at $U_j < 0.8$, the fluid forces of UC and DC changed slightly but decreased sharply at $U_j = 0.8$. When the flow velocity reached $U_j = 1.0$, the mean drag of the UC is virtually unaltered, the fluctuating lift approaches zero, and the C_D of the DC decreases by 17% and the C_L' by 99%.

For the jet velocity of $U_j = 1.0$ case, which was determined as the optimal control at Re=100, we conducted a comparison with the baseline case at various Reynolds numbers (Re = 75, 100, 125, 150, 175, 200). For all these Reynolds numbers, the jet flow with $U_j = 1.0$ suppresses violent vortex shedding, thus reduces the C_D and the C_L'.

The global flow structure almost remained unchanged at lower jet velocities. However, for the jet velocity of $U_j = 1.0$ case, the jet flow strips the shear layers from the surface of the UC on the near-wake side of the UC, thereby breaking the vortex and making a stable flow structure.

The findings from the HODMD analysis indicate that the jet flow induces a substantial backwards shift in all modes relative to the baseline case. Additionally, the mode energy decreases substantially, demonstrating that the jet flow effectively inhibits vortex shedding.

References

Assi, G.R.; P.W. Bearman; and N. Kitney. 2009. Low drag solutions for suppressing vortex-induced vibration of circular cylinders. Journal of Fluids and Structures 25:666-675.

Baek, H. and G.E. Karniadakis. 2009. Suppressing vortex-induced vibrations via passive means. Journal of Fluids and Structures 25:848-866.

Boujo, E. 2021. Second-order adjoint-based sensitivity for hydrodynamic stability and control. Journal of fluid mechanics 920:A12.

Carmo, B.S. and J.R. Meneghini. 2006. Numerical investigation of the flow around two circular cylinders in tandem. Journal of Fluids and Structures 22:979-988.

Chen, G.-B.; W.-L. Chen; D.-L. Gao; and Z.-F. Yang. 2021. Active control of flow structure and unsteady aerodynamic force of box girder with leading-edge suction and trailing-edge jet. Experimental Thermal and Fluid Science 120:110244.

Cimbala, J.M. and S. Garg. 1991. Flow in the wake of a freely rotatable cylinder with splitter plate. AIAA journal 29:1001-1003.

Dai, X.; D. Xu; M. Zhang; and R.J. Stevens. 2022. A three-dimensional dynamic mode decomposition analysis of wind farm flow aerodynamics. Renewable energy 191:608-624.

Dehkordi, B.G.; H.S. Moghaddam; and H.H. Jafari. 2011. Numerical simulation of flow over two circular cylinders in tandem arrangement. Journal of Hydrodynamics 23:114-126.

Delassaux, F.; I. Mortazavi; E. Itam; V. Herbert; and C. Ribes. 2021. Sensitivity analysis of hybrid methods for the flow around the ahmed body with application to passive control with rounded edges. Computers & Fluids 214:104757.

Dong, S.; G. Triantafyllou; and G. Karniadakis. 2008. Elimination of vortex streets in bluff-body flows. Physical review letters 100:204501.

Fransson, J.H.; P. Konieczny; and P.H. Alfredsson. 2004. Flow around a porous cylinder subject to continuous suction or blowing. Journal of Fluids and Structures 19:1031-1048.

Fu, H. and D. Rockwell. 2005. Shallow flow past a cylinder: control of the near wake. Journal of fluid mechanics 539:1-24.

Gao, D.; G. Chen; W. Chen; Y. Huang; and H. Li. 2019. Active control of circular cylinder flow with windward suction and leeward blowing. Experiments in Fluids 60:1-17.

Gerrard, J. 1966. The mechanics of the formation region of vortices behind bluff bodies. Journal of fluid mechanics 25:401-413.

Giannetti, F. and P. Luchini. 2007. Structural sensitivity of the first instability of the cylinder wake. Journal of fluid mechanics 581:167-197.

Hemati, M.S.; M.O. Williams; and C.W. Rowley. 2014. Dynamic mode decomposition for large and streaming datasets. Physics of Fluids 26.

Huang, G.; Y. Dai; and C. Yang. 2022. Energy extraction in the dynamic modes of flow for airfoil's laminar separation flutter. Physics of Fluids 34.

Jukes, T.N. and K.-S. Choi. 2009. Long lasting modifications to vortex shedding using a short plasma excitation. Physical review letters 102:254501.

Khan, H.H.; M.D. Islam; Y.Y. Fatt; I. Janajreh; and M.M. Alam. 2022. Flow-induced vibration on two tandem cylinders of different diameters and spacing ratios. Ocean Engineering 258:111747.

Kwon, K. and H. Choi. 1996. Control of laminar vortex shedding behind a circular cylinder using splitter

plates. Physics of Fluids 8:479-486.
Le Clainche, S. and J.M. Vega. 2017. Higher order dynamic mode decomposition. SIAM Journal on Applied Dynamical Systems 16:882-925.
Leontini, J.S.; M.C. Thompson; and K. Hourigan. 2007. Three-dimensional transition in the wake of a transversely oscillating cylinder. Journal of fluid mechanics 577:79-104.
Li, C.Y.; K. Tim; and G. Hu. 2020. Dynamic Mode Decomposition on pressure flow field analysis: Flow field reconstruction, accuracy, and practical significance. Journal of Wind Engineering and Industrial Aerodynamics 205:104278.
Li, J. and M. Zhang. 2022. Reinforcement-learning-based control of confined cylinder wakes with stability analyses. Journal of fluid mechanics 932:A44.
Lin, J.-C.; Y. Yang; and D. Rockwell. 2002. Flow past two cylinders in tandem: instantaneous and averaged flow structure. Journal of Fluids and Structures 16:1059-1071.
Lin, J.; J. Towfighi; and D. Rockwell. 1995. Near-wake of a circular cylinder: control, by steady and unsteady surface injection. Journal of Fluids and Structures 9:659-669.
Maceda, G.Y.C.; Y. Li; F. Lusseyran; M. Morzyński; and B.R. Noack. 2021. Stabilization of the fluidic pinball with gradient-enriched machine learning control. Journal of fluid mechanics 917:A42.
Marquet, O.; D. Sipp; and L. Jacquin. 2008. Sensitivity analysis and passive control of cylinder flow. Journal of fluid mechanics 615:221-252.
Meliga, P.; G. Pujals; and E. Serre. 2012. Sensitivity of 2-D turbulent flow past a D-shaped cylinder using global stability. Physics of Fluids 24.
Min, C. and H. Choi. 1999. Suboptimal feedback control of vortex shedding at low Reynolds numbers. Journal of fluid mechanics 401:123-156.
Mizushima, J. and N. Suehiro. 2005. Instability and transition of flow past two tandem circular cylinders. Physics of Fluids 17.
Narendran, K. and R. Jaiman. 2019. Effect of near-wake jet on the lock-in of a freely vibrating square cylinder. Physics of Fluids 31.
Park, D.; D. Ladd; and E. Hendricks. 1994. Feedback control of von Kármán vortex shedding behind a circular cylinder at low Reynolds numbers. Physics of Fluids 6:2390-2405.
Qu, L.; C. Norberg; L. Davidson; S.-H. Peng; and F. Wang. 2013. Quantitative numerical analysis of flow past a circular cylinder at Reynolds number between 50 and 200. Journal of Fluids and Structures 39:347-370.
Rabiee, A.; M. Barzan; and A. Mohammadebrahim. 2021. Flow-induced vibration suppression of elastic square cylinder using windward-suction-leeward-blowing approach. Applied Ocean Research 109:102552.
Ren, F.; J. Rabault; and H. Tang. 2021. Applying deep reinforcement learning to active flow control in weakly turbulent conditions. Physics of Fluids 33.
Sharman, B.; F.-S. Lien; L. Davidson; and C. Norberg. 2005. Numerical predictions of low Reynolds number flows over two tandem circular cylinders. International journal for numerical methods in fluids 47:423-447.
Shi, X.-D. and L.-H. Feng. 2015. Control of flow around a circular cylinder by bleed near the separation points. Experiments in Fluids 56:1-17.
Singh, S. and S. Mittal. 2005. Flow past a cylinder: shear layer instability and drag crisis. International journal for numerical methods in fluids 47:75-98.
Singha, S. and K. Sinhamahapatra. 2010. High-resolution numerical simulation of low Reynolds number

incompressible flow about two cylinders in tandem.
Sumner, D.; M. Richards; and O. Akosile. 2005. Two staggered circular cylinders of equal diameter in cross-flow. Journal of Fluids and Structures 20:255-276.
Wang, C.; H. Tang; F. Duan; and C. Simon. 2016. Control of wakes and vortex-induced vibrations of a single circular cylinder using synthetic jets. Journal of Fluids and Structures 60:160-179.
Wang, Y.; E. Ferrer; J. Saavedra; G. Paniagua; and E. Valero. 2021. Stability-analysis-based optimization to control flow separation over a diffusing passage. Physics of Fluids 33.
Wen, J.; L. Zhou; and H. Zhang. 2023. Mode interpretation of blade number effects on wake dynamics of small-scale horizontal axis wind turbine. Energy 263:125692.
Williams, D.R.; H. Mansy; and C. Amato. 1992. The response and symmetry properties of a cylinder wake subjected to localized surface excitation. Journal of fluid mechanics 234:71-96.
Wu, J. and C. Shu. 2011. Numerical study of flow characteristics behind a stationary circular cylinder with a flapping plate. Physics of Fluids 23.
Xu, G. and Y. Zhou. 2004. Strouhal numbers in the wake of two inline cylinders. Experiments in Fluids 37:248-256.
Zhang, H.; D. Xin; J. Zhan; and L. Zhou. 2021. Flow past a transversely oscillating cylinder at lock-on region and three-dimensional Floquet stability analysis of its wake. Physics of Fluids 33.
Zhang, H.; L. Zhou; P. Deng; and T.K. Tse. 2022. Fluid–structure-coupled Koopman mode analysis of free oscillating twin-cylinders. Physics of Fluids 34.
Zhang, H.; L. Zhou; and K. Tim. 2022. Mode-based energy transfer analysis of flow-induced vibration of two rigidly coupled tandem cylinders. International Journal of Mechanical Sciences 228:107468.
Zhou, L.; H. Li; K. Tim; X. He; G.Y.C. Maceda; and H. Zhang. 2023. Sensitivity-aided active control of flow past twin cylinders. International Journal of Mechanical Sciences 242:108013.
Zhu, H.; J. Yao; Y. Ma; H. Zhao; and Y. Tang. 2015. Simultaneous CFD evaluation of VIV suppression using smaller control cylinders. Journal of Fluids and Structures 57:66-80.
Zhu, Q.; L. Zhou; J. Wen; T. Liu; J. Zhang; H. Tang; and H. Zhang. 2023. Laminar flow over a rectangular cylinder experiencing torsional flutter: Dynamic response, forces and coherence modes. Physics of Fluids 35.